Journal of Molecular Catalysis A: Chemical 376 (2013) 1–6

Contents lists available at SciVerse ScienceDirect

Journal of Molecular Catalysis A: Chemical

journal homepage: www.elsevier.com/locate/molcata

Controllable preparation of $BiFeO_3$@carbon core/shell nanofibers with enhanced visible photocatalytic activity

Yi Liu, Ruzhong Zuo*, Shishun Qi

Institute of Electro Ceramics & Devices, School of Materials Science and Engineering, Hefei University of Technology, Hefei 230009, China

ARTICLE INFO

Article history:
Received 19 January 2013
Received in revised form 1 April 2013
Accepted 6 April 2013
Available online xxx

Keywords:
Electrospining
Hydrothermal synthesis
$BiFeO_3$@carbon nanofibers
Photocatalyst

ABSTRACT

$BiFeO_3$@carbon core/shell nanofibers (BFO@C NFs) with different thickness of carbon layers were successfully prepared by combining the electrospining technique and hydrothermal process. Scanning electron microscopy and transmission electron microscopy were employed to characterize the products. The results demonstrated that a uniform carbon layer was coated on the surface of BFO NFs. It was proposed that the introduction of carbon should not only enhance the light absorption of BFO NFs and the adsorption capacity for methyl orange, but also facilitate the separation of photogenerated electron–hole pairs, both of which result in the enhanced photocatalytic activity of BFO NFs. In addition, BFO@C NFs are stable under visible light irradiation and could be easily recycled, indicating that they can be used as effective photocatalysts under visible light.

1. Introduction

In recent years, visible-light-driven photocatalysts have been developed for efficient utilization of solar energy to address the increasing environmental pollution and energy problems. To date, a large number of metal oxides as photocatalyst have been explored for the purpose of efficient degradation of harmful organic substances and hydrogen production through decomposing water. In particular, the TiO_2 photocatalyst is widely employed in the environmental cleaning by degrading organic pollutants and hydrogen production by decomposing water, due to their excellent photochemical stability, low cost, and non-toxicity [1,2]. However, for practical applications, TiO_2 is not a good candidate in the visible-light region, because it only absorbs ultraviolet light of no longer than 387.5 nm for the anatase phase and 413.3 nm for the rutile phase. Although many efforts have been devoted to enhancing the photocatalytic efficiency and visible light utilization of TiO_2 by modifying TiO_2 with metals, non-metals, semiconductor oxides, and photo-sensitizers [3–10], the corresponding photocatalytic efficiency is still not ideal for practical applications. From the viewpoint of using solar energy, it is of great interest to develop efficient visible-light photocatalysts for the photodegradation of organic pollutants.

Bismuth ferrites are a very important family of inorganic materials that have received increasing attention because of their potential utilization in sensing, actuation, and digital memory [11,12]. As a typical bismuth ferrite, $BiFeO_3$ (BFO) as one of the well-known multiferroic compounds with ferroelectricity and magnetic ordering [13], has a rhombohedrally distorted perovskite structure with a space group R3c [14]. This material has attracted a great deal of attention due to its possible applications as nanogenerators, ferroelectric random access memory devices, and ferroelectric diodes [15]. In addition, BFO is also an important visible-light-driven photocatalyst owing to its narrow band-gap energy (2.2 eV). Recently, BFO has proven to be capable of degrading organic contaminants [16]. Additionally, it has been reported that $SrTiO_3$-coated BFO nanoparticles can decompose water into H_2 and O_2 under UV- or visible-light irradiation [17]. Many efforts have been made to improve the photocatalytic performance of BFO material. The design and morphological control on crystal facets of BFO is one of the most important ways to optimize its photocatalytic activity. Fei et al. demonstrated that BFO pills with highly exposed $\{1\,1\,1\}_c$ facets show an obviously enhanced visible light response [18]. Huo et al. reported that BFO hollow microspheres with large surface area synthesized via a solvethermal process exhibit high photocatalytic activity for methyl blue degradation under visible-light irradiation [19].

The basic principle of semiconductor photocatalysis involves the migration of photogenerated electrons (e^-) and holes (h^+) to the surface serving as redox sources and the destruction of pollutants [1]. Another current bottleneck in photocatalysis is the poor quantum yield owing to a rapid recombination rate of the photogenerated electron–hole pairs, which tends to limit the practical application of photocatalysis. It has been reported that nanostructured BFO/TiO_2 composites could enhance the photocatalytic performance by improving the photo-generated electron–hole

* Corresponding author. Tel.: +86 551 62905285; fax: +86 551 62905285.
E-mail address: piezolab@hfut.edu.cn (R. Zuo).

1381-1169/$ – see front matter © 2013 Elsevier B.V. All rights reserved.
http://dx.doi.org/10.1016/j.molcata.2013.04.005

separation and enhancing the interfacial charge transfer efficiency [20]. In addition, the $SrTiO_3$-coated BFO material exhibited enhanced visible-light photocatalytic activity as well [17].

As well known, functional carbonaceous materials could serve as an intercomponent deposited on the surface of polymers, ceramics, metals, and oxides with the purpose of modifying the corrosion resistance, thermal stability, adsorbability, or electronic properties of these materials. It has been reported that the photocatalytic property of the materials can be improved by modifying with carbon [6,21–24]. Recently, grapheme/BFO nanocomposities have been reported, which show enhanced optical absorption property [25]. However, to the best of our knowledge, the synthesis of BFO@carbon core/shell photocatalysts with efficient electron–hole separation ability has never been reported. Herein, we reported a BFO@carbon core/shell nanofibers (BFO@C NFs) by combining electrospinning technique and hydrothermal process. The influence of carbon on the photocatalytic activity of BFO@C NFs was investigated by decomposing methyl orange solution (MO). And the mechanism of the photocatalysis enhancement in the BFO@C NFs was proposed as well.

2. Experimental

2.1. Fabrication of BFO nanofibers

Firstly, a sol–gel solution, referred to as solution A, was prepared by dissolving 3.027 g of $Bi(NO_3)_3{\cdot}5H_2O$ and 2.424 g of $Fe(NO_3)_3{\cdot}9H_2O$ in 22 mL of 2-methoxyethanol. The solution pH value was adjusted to 4.0 by adding drops of ethanolamine. Then, 6 mL of glacial acetic acid was added to control the solution viscosity. The solution was stirred for 12 h at room temperature. The second solution, referred to as solution B, was prepared by adding 1 g of polyvinyl pyrrolidone (PVP, M = 1 300 000, Aladdin) to 10 mL of dimethyl formamide (DMF)/ethanol (1:1) solvent mixture. The solution B was magnetically stirred for about 1 h. Subsequently, 5 mL of solution A was added to the solution B drop by drop under constant stirring and homogeneous BFO precursor solution for electrospinning was obtained. All raw materials are analytic purity without further purification. Finally, the obtained precursor was transferred to a plastic syringe and fed by a micro-infusion pump to the stainless steel needle at a rate of 0.4 mL/h. The electrospinning setup we used was a horizontal one with a rotating drum as a collector. A DC voltage of 16 kV was applied to the needle and the distance was 14 cm from the needle to the collector. The fiber mats were collected on the aluminum foil wrapped on the drum. The ultimate samples were obtained by drying at 120 °C for 6 h and then annealed at 550 °C for 2 h in argon atmosphere.

2.2. Preparation of BFO@C NFs

In a typical procedure, BFO@C NFs were prepared by a hydrothermal process. Firstly, glucose (0.16 g) and BFO NFs (25 mg) were put into a Teflon-lined stainless steel autoclave of 40 mL capacity containing 32 mL of deionized water to make a glucose solution with a concentration of 5 g/L. After vigorous stirring for 10 min, the suspension mixture was then sealed and heated at 180 °C for 4 h. After the end of the reaction, the autoclave was cooled to ambient temperature naturally. The products were collected using a centrifuge and then washed with water and ethanol several times. Finally, the samples were dried at 70 °C for 6 h. These samples prepared with different concentrations of glucose (5, 15 and 30 g/L) were denoted as S1, S2 and S3, respectively. In addition, pure BFO NFs was denoted as S0.

2.3. Characterization

The products were analyzed by an X-ray diffractometer (XRD, D/Max-RB, Rigaku, Japan) with a Cu Kα radiation in a 2θ range from 10° to 70°. The product morphology was investigated by means of a scanning electron microscope (SEM, SU8020, Hitachi, Japan) equipped with an energy-dispersive X-ray spectrometer (EDX) and a transmission electron microscope (TEM, JEM-2100F, JEOL, Japan, operated at an accelerating voltage of 200 kV). UV–vis diffuse reflectance spectra of the samples were measured using barium sulfate as a standard material by a UV–vis spectrophotometer (TU-1950, Beijing Perkinje General Instrument Co., Ltd., Beijing, China) with an integrating sphere. The specific surface areas of the as-prepared samples were determined according to Brunauer–Emmett–Teller (BET) method on nitrogen adsorption at 77 K by using a TriStar II 3020M analyzer (Micromeritics Co., USA). The room temperature photoluminescence spectra (PL) were performed on a fluorescence spectrophotometer (F-4600, Hitachi, Japan) with the excitation wavelength of 210 nm. The photocatalytic activity of the BFO NFs and BFO@C NFs samples was evaluated under irradiation of a 400 W metal-halide lamp ($\lambda > 410$ nm) at natural pH value. The initial concentration of MO was 20 mg L^{-1} with a catalyst loading of 0.5 g/L. Before illumination, the solution was stirred for 30 min in the dark in order to reach the adsorption–desorption equilibrium between the photocatalyst and MO. After 1 h, a small quantity of the solution was taken, and the concentration of MO was determined by measuring the value at about 464 nm using a UV–vis spectrophotometer. Each time before the absorption measurement, the sample solution was centrifuged for 30 min to separate the catalyst powder from the solution. The absorption was converted to the MO concentration referring to a standard curve showing a linear behavior between the concentration and the absorption at this wavelength.

3. Results and discussion

3.1. SEM of the as-prepared composite nanofibers

The morphologies of the as-obtained pure BFO NFs (S0) and BFO@C NFs (S2) were representatively characterized by SEM. It could be observed from Fig. 1a that these randomly oriented BFO NFs have a continuous and coarse surface microstructure. The average diameter of the as-prepare BFO NFs is 90 ± 40 nm. After a hydrothermal treatment, the non-woven nanofibrous morphology of the BFO NFs was remained, as shown in Fig. 1b. Although there is no change in the fiber diameter, it can be seen that the surface of the BFO@C NFs becomes more smooth, which can be attributed to the carbon coated on the surface of nanofibers. EDX analysis performed on individual nanofiber of S2 revealed that the S2 sample is composed of Bi, Fe, O and C (Fig. 1c). Furthermore, its chemical composition conforms to the Bi/Fe atomic ratio of ~1.07:1, which hints the presence of BFO.

3.2. TEM of the as-prepared composite nanofibers

The morphology and fine structure of the BFO NFs and BFO@C NFs products were further examined by TEM. Fig. 2a showed the TEM image of the BFO NFs (S0) and their average diameter was measured to be ~90 nm, which confirms the diameter distribution estimated from the SEM images. Fig. 2b displayed the typical TEM image of the S1 sample. It can be seen from the inset that a carbon layer with a thickness of 1.5 nm was coated on the surface of BFO NFs uniformly. Similar results could be observed in the TEM images of S2 and S3 (Fig. 2c and d). In addition, it is clear that there exists a well-developed interface between the BFO nanofiber and

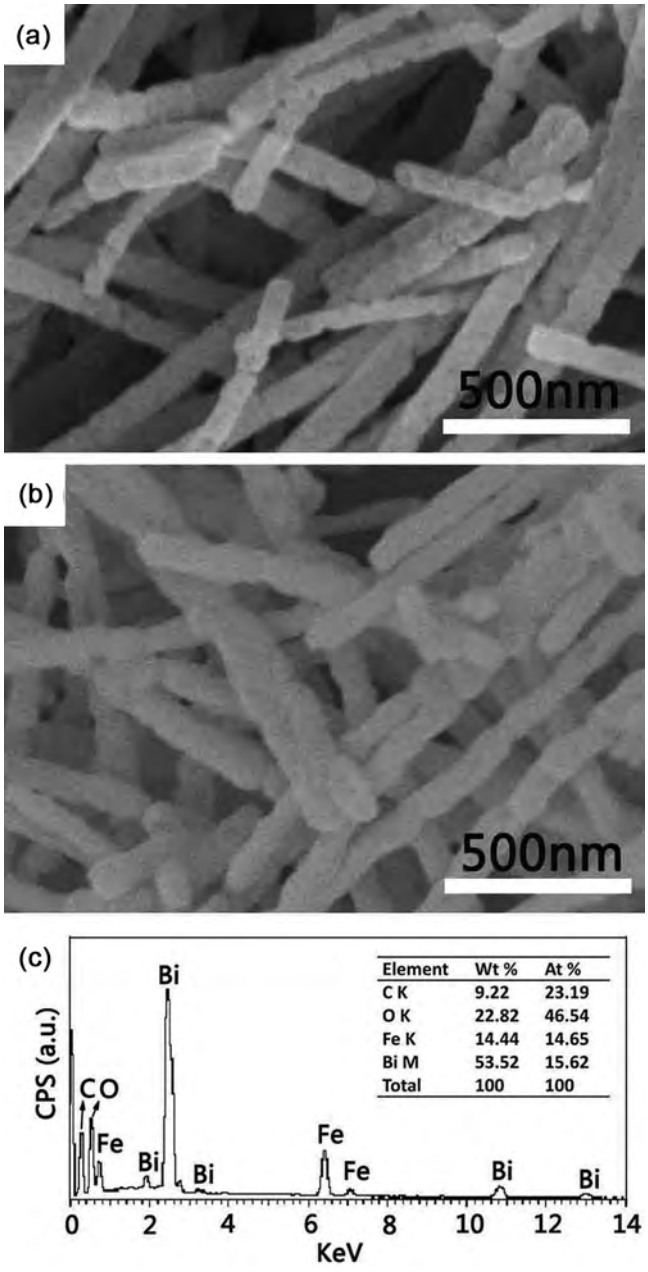

Fig. 1. SEM images of the as-prepared samples: (a) BFO NFs (S0) and (b) BFO@C NFs (S2); (c) EDX pattern of the S2 sample.

the carbon layer. And the thickness of carbon layer increased to 3 and 6 nm for the S2 and S3 samples as the amount of glucose was further increased to 15 and 30 g/L, respectively. Fig. 2e showed a high-resolution TEM image of the interface between BFO and carbon in the S2 sample corresponding to the marked area of Fig. 2c. It could be seen that S2 exhibits a typical core/shell structure with a carbon layer thickness of 3 nm. In addition, the TEM image in Fig. 2e exhibited a continuous lattice strip and an interplanar spacing of 0.277 nm was calculated corresponding to the (1 1 0) planes of the rhombohedral BFO.

3.3. Phase structure

The crystalline structure and phase purity of BFO fibers were characterized by XRD, as shown in Fig. 3. All of the diffraction peaks of the S0 sample could be assigned to the rhombohedrally distorted perovskite structure of BFO (JCPDS 71-2494), and no impurity peaks were observed, indicating that phase pure perovskite BFO could be obtained by annealing at 550 °C in an argon atmosphere. The strong and sharp diffraction peaks of S0 suggest that BFO NFs were well crystallized. The XRD patterns of S1, S2 and S3 displayed the diffraction peaks of pure BFO as well. However, the graphitic carbon peak at $2\theta = 25.6^\circ$ is too weak to see [26], which might be ascribed to the small amount of carbon [21]. In addition, according to the X-ray line-broadening of the (0 1 2) diffraction peak using the Debye–Scherrer formula, the average grain size of BFO NFs were calculated to be ~25 nm for S0, S1, S2 and S3.

3.4. UV–vis diffuse reflectance spectra

The optical absorption property of the BFO NFs (S0) and BFO@C NFs (S1, S2 and S3) was measured by UV–vis absorption spectra transformed from the corresponding diffuse spectra according to the well-known Kubelka–Munk theory [27], and the results are shown in Fig. 4. It is clear that a broad absorption band in the range of 410–570 nm was observed in the absorption spectra of the BFO NFs (S0), which indicates that BFO can absorb considerable amounts of visible light in this range. Notably, after the hydrothermal treatment with glucose, all BFO@C NFs (S1, S2 and S3) can adsorb more light in the 410–800 nm regions than pure BFO. Moreover, the absorption edges of all BFO@C NFs samples (S1, S2 and S3) have a little shift to long wavelength, indicating almost the same band gap energy as that of BFO NFs (S0). This keeps consistence with the previous reports where no change in band gap energy was observed for carbon coated ZnO [21] and Zn_2TiO_4 [24]. In the present work, most of the carbon in the BFO@C NFs samples was free, graphitic carbon, hence broad background absorption in the visible-light region dominated the UV–vis spectra. In addition, the absorption of the BFO@C NFs samples increases with increasing the carbon content. The possible reason for the improved absorption of visible-light may be ascribed to two aspects. One should originate from the carbon in the sample, which could enhance the absorption in the whole visible region; the other was the introduction of the carbon may modify the fundamental process of electron–hole pair formation and result in an increased electric surface charge of the oxide within the composite. This result demonstrated that BFO@C NFs materials may exhibit increased photocatalytic activity in the visible-light region.

3.5. Photocatalytic activities

The visible-light photocatalytic activity of the BFO NFs (S0) and BFO@C NFs samples (S1, S2 and S3) was evaluated by using them to degrade the MO solution. Fig. 5a shows the photodegradation efficiency of the MO solution for BFO NFs and BFO@C NFs samples under visible-light irradiation. The experiments conducted in dark condition demonstrated that the adsorption–desorption equilibrium between the photocatalyst and MO could be established within 30 min. It can be seen that the adsorption capacity of BFO@C NFs for MO was significantly enhanced, which may result from the good adsorbability of amorphous carbon. In addition, all BFO@C NFs samples (S1, S2 and S3) exhibit higher degradation efficiency for MO than the pure BFO NFs (S0), and S2 shows the highest visible-light-driven photocatalytic property. For a better comparison of the photocatalytic efficiency of the BFO NFs (S0) and BFO@C NFs samples (S1, S2 and S3), the reaction rates for MO photocatalytic degradation for all samples are estimated in Fig. 5b. It is evident that the plot of $\ln(C/C_0)$ versus time is close to a liner curve, indicating that the photodegradation of MO follows the first-order reaction kinetics. The degradation constants (k) were calculated to be 0.194, 0.287, 0.648 and 0.485 h^{-1} for S0, S1, S2 and S3, respectively. Obviously, with an increase in the content of

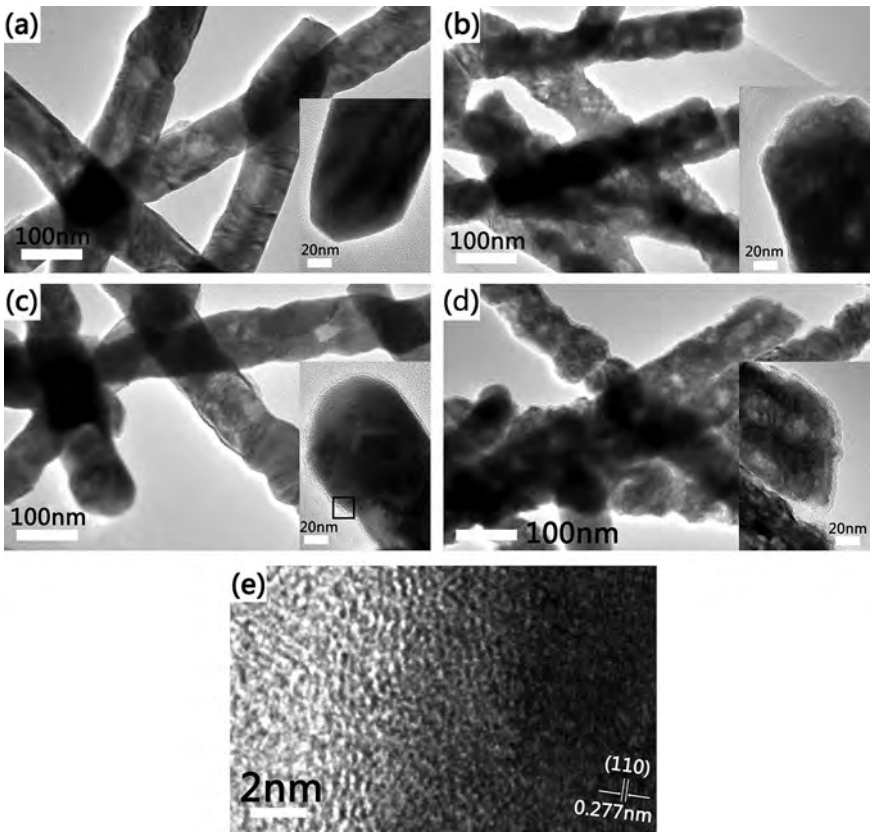

Fig. 2. TEM images of the as-prepared samples: (a) S0, (b) S1, (c) S2, (d) S3, and (e) high-resolution TEM image of the S2 sample; the inset in each figure corresponds to the enlarged TEM images of S0, S1, S2 and S3.

the deposited carbon, the photocatalytic efficiency of BFO@C NFs samples first increased and then decreased, which is consistent with the activity discussed above. It is supposed that the BFO NFs coated with a thicker carbon layer may block the inherent optical absorption, result in a decrease of the quantity of photogenerated charges, and lower the photoactivity. In addition, excessive carbon deposition may result in more limited MO molecules close to the surface of BFO where MO molecular were decomposed by hydroxyl radicals ($OH^{\bullet}$) yielded by the holes, which may also attributed to the decreased photoactivity [22].

It is worth pointing out that the stability of a given photocatalyst during photoreaction is a crucial issue for long-term use in practical applications. Consequently, two factors needed to be considered: (i) the ease with which the catalyst could be separated from solution. In this work, the composite samples were of nanofibrous morphology and could be easily separated from an aqueous suspension; and (ii) the stability of the catalyst to maintain its high activity over time. Fig. 6 shows the recycled experiments of the photodegradation of MO over S2 for three cycles (3 h visible-light irradiation for each cycle). It was observed that the photodegradation rate remained constant over three consecutive cycles, indicating that the as-prepared photocatalyst is stable under visible-light irradiation. This result demonstrated the industrial potential of BFO@C NFs samples as a visible-light-driven photocatalyst.

3.6. Photocatalytic mechanism

It has been generally accepted that the photocatalytic performance of photocatalysts is closely related with their crystallite

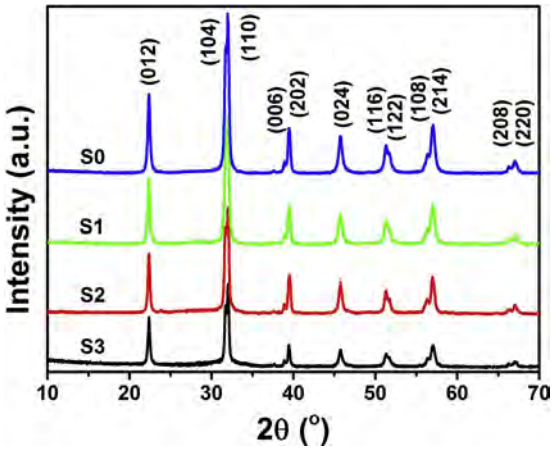

Fig. 3. XRD patterns of the S0, S1, S2 and S3 samples.

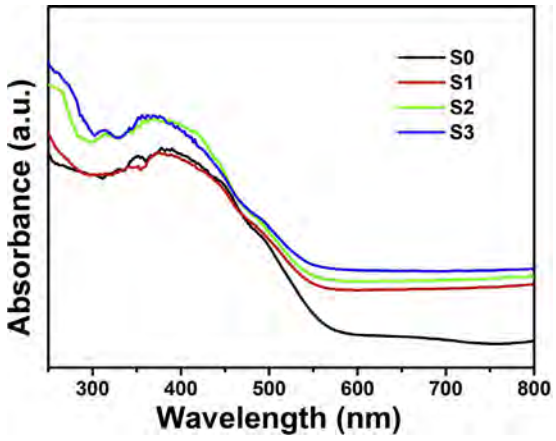

Fig. 4. UV–vis absorption spectra of the S0, S1, S2 and S3 samples.

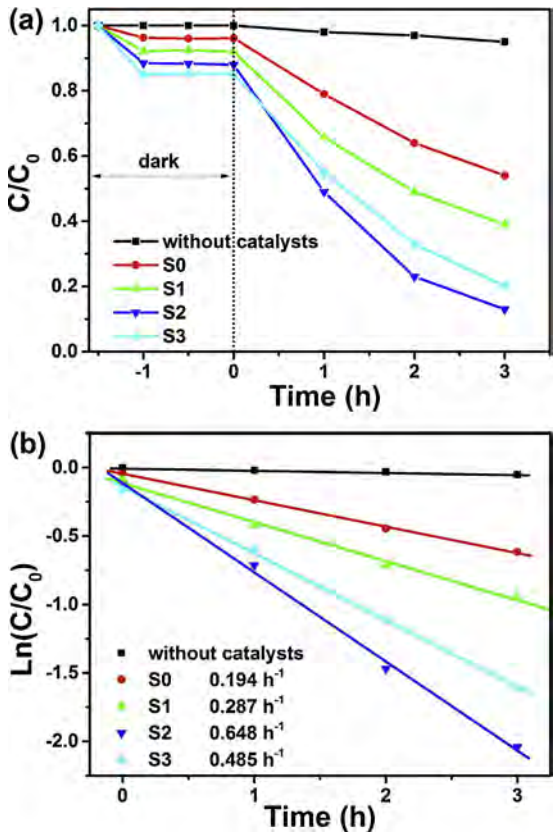

Fig. 5. (a) Degradation of MO using S0, S1, S2 and S3 under visible light irradiation; (b) kinetic linear simulation curves of S0, S1, S2 and S3.

size, phase structure, crystallinity, morphology, surface area, optical absorption and separation efficiency of photogenerated electron–hole pairs. The XRD results reveal that the crystallite size, crystal structure and crystallinity of the BFO NFs remained similar after the hydrothermal treatment, meaning that they would not be the reason for the big discrepancy in photocatalytic performance of these samples. Moreover, no significant differences in the BET surface area were observed between S0 (23.12 m^2/g) and S2 (27.43 m^2/g), so we rule out surface areas as the main factor to influence their photocatalytic activity. Therefore, the improvement of photocatalytic activity more likely resulted from the following reasons: Firstly, it is evident that the coating of the carbon layer enhances the absorption of BFO NFs in the visible-light region

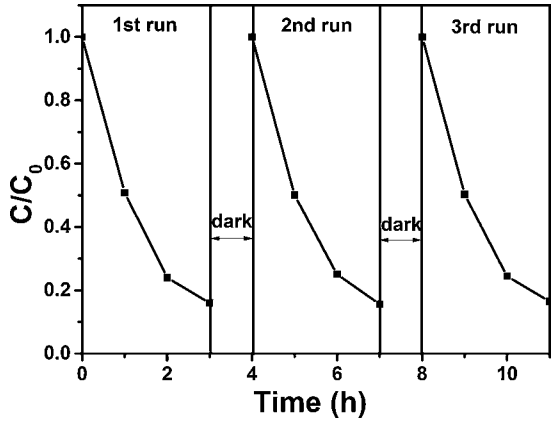

Fig. 6. Cycling runs in photocatalytic degradation of MO in the presence of the S2 sample under visible light irradiation.

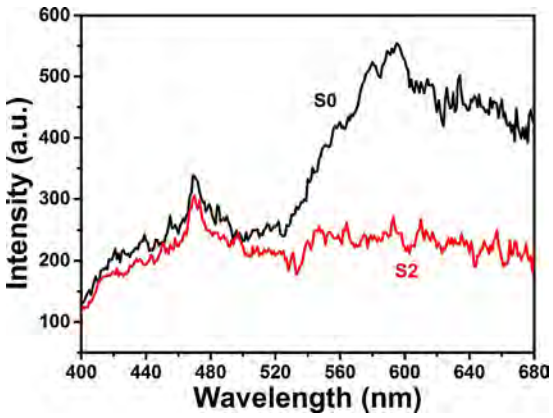

Fig. 7. PL spectra of the S0 and S2 samples.

(Fig. 4), demonstrating that more photons can be absorbed and be utilized for the photocatalytic reaction. Secondly, since the amorphous carbon has good adsorbability, the adsorption capacity of BFO@C NFs for MO was significantly enhanced, resulting in an increase of the rate of photocatalytic reaction. Finally, the introduced carbon may provide a network to collect and rapidly transfer the photoexcited electrons from the conduction band of BFO during the photocatalytic process, which reduces the recombination probability between photoexcited electrons and holes and leaves more holes for the oxidization reaction of the adsorbed MO. To confirm the decreased recombination of electron–hole pairs in BFO@C NFs, room temperature PL emission spectra of the S0 and S2 samples were measured, as shown in Fig. 7. It can be seen that the PL spectrum of BFO (S0) shows a strong emission, which indicates that the electrons and holes recombine rapidly. By contrast, the BFO@C NFs (S2) sample displays a drastic decrease in emission intensity, indicating that the recombination rate of electron–hole pairs was very slow. Therefore, it is supposed that the introduction of carbon can facilitate the separation of photogenerated electron–hole pairs and enhance the photocatalytic degradation efficiency.

4. Conclusions

The BFO@C NFs were synthesized through a combination of electrospinning technique and hydrothermal process in the presence of glucose. The thickness of the carbon layer could be controlled by adjusting the concentration of glucose in hydrothermal process. The investigation of optical absorption and photocatalytic activity demonstrated that the BFO@C NFs samples showed significantly higher photocatalytic activity than BFO NFs on the degradation of MO under visible-light irradiation. It was found that the presence of carbon layers not only significantly enhance the light absorption of BFO NFs and adsorption capacity for MO, but also facilitate the separation of photogenerated electron–hole pairs, which results in an increased photocatalytic degradation efficiency. In addition to the high photocatalytic activity, BFO@C NFs samples could be easily recycled without an obvious decrease of photocatalytic activity, demonstrating the potential of BFO@C NFs as a visible-light-driven photocatalyst.

Acknowledgments

This work was financially supported by funding from the Natural Science Foundation of Anhui Province (1108085J14) and the National Natural Science Foundation of China (51272060).

References

[1] M.A. Fox, M.T. Dulay, Chem. Rev. 93 (1993) 341–357.
[2] M.R. Hoffmann, S.T. Martin, W. Choi, D.W. Bahnemann, Chem. Rev. 95 (1995) 69–96.
[3] H. Yamashita, M. Harada, J. Misaka, M. Takeuchi, B. Neppolian, M. Anpo, Catal. Today 84 (2003) 191–196.
[4] M. Anpo, M. Takeuchi, J. Catal. 216 (2003) 505–516.
[5] R. Asahi, T. Morikawa, T. Ohwaki, K. Aoki, Y. Taga, Science 293 (2001) 269–271.
[6] L. Zhao, X.F. Chen, X.C. Wang, Y.J. Zhang, W. Wei, Y.H. Sun, M. Antonietti, M.-M. Titirici, Adv. Mater. 22 (2010) 3317–3321.
[7] S.S. Qian, C.S. Wang, W.J. Liu, Y.H. Zhu, W.J. Yao, X.H. Lu, J. Mater. Chem. 21 (2011) 4945–4952.
[8] W. Zhao, Y.L. Sun, F.N. Castellano, J. Am. Chem. Soc. 130 (2008) 12566–12567.
[9] G.P. Dai, S.Q. Liu, Y. Liang, H.J. Liu, Z.C. Zhong, J. Mol. Catal. A: Chem. 368/369 (2013) 38–42.
[10] M. Hojamberdiev, G.G. Zhu, P. Sujaridworakun, S. Jinawath, P. Liu, J.P. Zhou, Powder Technol. 218 (2012) 140–148.
[11] J. Wang, J.B. Neaton, H. Zheng, V. Nagarajan, S.B. Ogale, B. Liu, D. Viehland, V. Vaithyanathan, D.G. Schlom, U.V. Waghmare, N.A. Spaldin, K.M. Rabe, M. Wuttig, R. Ramesh, Science 299 (2003) 1719–1722.
[12] M. Valant, D. Suvorov, Chem. Mater. 14 (2002) 3471–3476.
[13] Y.P. Wang, L. Zhou, M.F. Zhang, X.Y. Chen, J.M. Liu, Z.G. Liu, Appl. Phys. Lett. 84 (2004) 1731–1733.
[14] F. Kubel, H. Schmid, Acta Crystallogr. B 46 (1990) 698–702.
[15] G. Catalan, J.F. Scott, Adv. Mater. 21 (2009) 2463–2485.
[16] F. Gao, X.Y. Chen, K.B. Yin, S. Dong, Z.F. Ren, F. Yuan, T. Yu, Z.G. Zou, J.M. Liu, Adv. Mater. 19 (2007) 2889–2892.
[17] J.H. Luo, P.A. Maggard, Adv. Mater. 18 (2006) 514–517.
[18] L.F. Fei, J.K. Yuan, Y.M. Hu, C.Z. Wu, J.L. Wang, Y. Wang, Cryst. Growth Des. 11 (2011) 1049–1053.
[19] Y.N. Huo, Y. Jin, Y. Zhang, J. Mol. Catal. A: Chem. 331 (2010) 15–20.
[20] S. Li, Y.H. Lin, B.P. Zhang, J.F. Li, C.W. Nan, J. Appl. Phys. 105 (2009) 054310.
[21] Y. Guo, H.S. Wang, C.L. He, L.J. Qiu, X.B. Cao, Langmuir 25 (2009) 4678–4684.
[22] P. Zhang, C.L. Shao, Z.Y. Zhang, M.Y. Zhang, J.B. Mu, Z.C. Guo, Y.C. Liu, Nanoscale 3 (2011) 2943–2949.
[23] J.G. Hou, S.Q. Jiao, H.M. Zhu, R.V. Kumar, CrystEngComm 13 (2011) 4735–4740.
[24] P. Zhang, C.L. Shao, M.Y. Zhang, Z.C. Guo, J.B. Mu, Z.Y. Zhang, X. Zhang, P.P. Liang, Y.C. Liu, J. Hazard. Mater. 229/230 (2012) 265–272.
[25] T. Li, J.F. Shen, N. Li, M.X. Ye, Mater. Lett. 91 (2013) 42–44.
[26] L.X. Yang, S.L. Luo, S.H. Liu, Q.Y. Cai, J. Phys. Chem. C 112 (2008) 8939–8943.
[27] P. Kubelka, F. Munk, Z. Tech. Phys. 12 (1931) 593–601.